



HAL
open science

In-situ X-ray tomographic study of the morphological changes of a Si/C paper anode for Li-ion batteries

V. Vanpeene, A. Etienne, A. Bonnin, E Maire, L. Roué

► To cite this version:

V. Vanpeene, A. Etienne, A. Bonnin, E Maire, L. Roué. In-situ X-ray tomographic study of the morphological changes of a Si/C paper anode for Li-ion batteries. *Journal of Power Sources*, 2017, 350, pp.18-27. 10.1016/j.jpowsour.2017.03.044 . hal-03515687

HAL Id: hal-03515687

<https://hal.science/hal-03515687>

Submitted on 6 Jan 2022

HAL is a multi-disciplinary open access archive for the deposit and dissemination of scientific research documents, whether they are published or not. The documents may come from teaching and research institutions in France or abroad, or from public or private research centers.

L'archive ouverte pluridisciplinaire **HAL**, est destinée au dépôt et à la diffusion de documents scientifiques de niveau recherche, publiés ou non, émanant des établissements d'enseignement et de recherche français ou étrangers, des laboratoires publics ou privés.

**In-situ X-ray tomographic study of the morphological changes of a Si/C paper anode
for Li-ion batteries**

V. Vanpeene ^{a,b}, A. Etienne ^b, A. Bonnin ^c, E. Maire ^{b,*} L. Roué ^{a,*}

^a *INRS- Énergie, Matériaux, Télécommunications, Varennes, Québec, J3X 1S2, Canada.*

^b *Univ Lyon, INSA-Lyon, MATEIS CNRS UMR5510, F-69621 Villeurbanne, France*

^c *Swiss Light Source, Paul Scherrer Institute, 5232 Villigen, Switzerland*

* Corresponding authors:

E-mail: eric.maire@insa-lyon.fr (E. Maire), lionel.roue@emt.inrs.ca (L. Roué)

ABSTRACT

The evolution of the three-dimensional (3D) morphology of a Si-based electrode upon cycling (1st discharge, 1st charge and 2nd discharge) is studied by *in-situ* synchrotron X-ray tomography. The Si-based electrode is constituted of silicon/carbon black/carboxymethylcellulose (Si/CB/CMC) embedded in a commercial carbon fiber paper, acting as a flexible 3D current collector. Its initial areal discharge capacity is 4.9 mAh cm⁻². A reconstructed volume of 293 × 293 × 137 μm³ is analyzed with a resolution of ~0.3 μm. Three phases are identified: (i) the solid phase (C fibers + Si + CB + CMC), (ii) the electrolyte phase (pores filled with electrolyte) and (iii) the gas phase (electrolyte-free pores). Their respective volume fraction, size distribution and connectivity, and also the dimensional changes of the electrode along the three axes are quantified during cycling. At the beginning of the 1st discharge (lithiation), the formation of gas channels attributed to the reductive electrolyte decomposition is observed. During the 1st charge, large cracks are formed through the electrode, which reclose during the subsequent discharge. The electrode expansion/contraction due to the Si volume change is partially irreversible, occurs mainly in the transverse direction and is much larger in the bottom part of the electrode.

Keywords: Li-ion batteries; silicon anode; *in situ* X-ray tomography; 3D morphology.

1. Introduction

One of the biggest technological challenges facing the human race is probably to secure its future access to carbon free energy. Renewable energy is part of the solution to secure this access provided that we improve our ability to store this energy. The Li-ion battery is one of the most efficient technologies for electric energy storage. However, the energy density needs to be enhanced, especially for transport applications, and for that purpose alternative electrode materials must be considered. In this context, silicon is a very promising anode material due to its high theoretical gravimetric capacity of 3579 mAh g⁻¹ (Li₁₅Si₄) compared to the 372 mAh g⁻¹ of graphite (LiC₆) [1,2]. However, it is very challenging to obtain stable Si-based anodes due to the large volume change of silicon during its lithium alloying (up to ~280% for Li₁₅Si₄) [1,3], which induces the disintegration (cracking, peeling-off) of the electrode, and leads to the instability of the solid electrolyte interphase (SEI). In the last years, different strategies have been evaluated to solve these issues, especially by using nanosized Si materials (nanoparticles, nanowires, nanocomposites, nanoporous structures, thin films...) [4-6], which are able to accommodate a large volume change without extensive cracking. The production of such materials at low cost and large scale as required for commercial implementation is however challenging. Moreover, their high surface area, which enhances SEI reactions and related irreversible Li consumption, and their low compactness resulting in low volumetric and areal electrode capacities are major drawbacks for their practical application.

We have recently shown that the cycle life and power performance of micrometric Si-based electrodes with large Si mass loadings (up to 10 mg Si cm⁻²) can be greatly improved by using a copper foam (3D geometry) instead of conventional copper foil (2D geometry) as the current collector [7]. The small thickness of the composite Si coating on the Cu foam walls compared to that on a flat Cu substrate is assumed to favor a better preservation of the electronic wiring upon cycling. As a result, we have shown that an areal electrode capacity as high as 10 mAh cm⁻² can be maintained for more than 400 cycles. However, our calculation based on a virtual stack consisting of a Si/Cu foam negative electrode and a LiFePO₄-based positive electrode indicates that thinner and lighter Cu foam

(e.g. $\leq 125\mu\text{m}$ thick rather than the $300\mu\text{m}$ thick Cu foam that was used) is required to get a significant gain in gravimetric and volumetric energy densities compared to the traditional $\text{LiFePO}_4/\text{graphite}$ cell. However, the production of thin ($<300\mu\text{m}$) and highly porous ($>80\%$) Cu foams is not an easy task.

In this context, the use of carbon fiber papers as 3D current collectors appears highly relevant since such materials are thinner and lighter than Cu foams in addition to being commercially available at low cost and large scale. For instance, these carbon papers have been commonly used for decades as gas diffusion layers for fuel cell applications. In the last years, various Si/3D carbon substrate architectures have been evaluated as anodes for Li-ion batteries but only a few studies have been published on Si materials supported on commercial carbon papers [8-10]. Moreover, the morphological evolution with cycling of such complex 3D microstructures has never been investigated in detail, which is essential for a better comprehension of their failure mechanisms and for optimizing their formulation and architecture.

In recent years, X-ray computed tomography (XRCT) has been used to characterize the porous microstructure of various Li-ion battery electrodes, including Si-based anodes [11-16]. However, these latter have been performed with a conventional electrode architecture (*i.e.* by casting the slurry on a 2D rigid current collector such as a steel or Cu rod) in contrast to the present study in which the slurry is embedded in a 3D and flexible C paper current collector. The XRCT technique permits 3D imaging of the analyzed electrodes with a quantification of key morphological parameters of the constitutive solid and pore phases (tortuosity, connectivity, volume fraction, size distribution...). Moreover, *in situ* acquisition can be performed with an appropriate setup in order to assess the morphological evolution of the electrode upon cycling. In a conical beam configuration, the XRCT spatial resolution is determined by the X-ray spot size, which depends on the X-ray source and the source-sample working distance. Micrometric spatial resolution is usually obtained with a conventional laboratory X-ray source whereas tens of nm resolution can be reached with a synchrotron X-ray source. The main limitation of the XRCT technique is the difficulty to distinguish

materials having low and/or similar X-ray attenuation coefficients. In that case, phase-contrast XRCT may be required [17].

In the present work, synchrotron XRCT analyses are performed to visualize and quantify the morphological changes occurring during the first lithiation/delithiation stage of a Si/C paper electrode. It is shown that major changes in the 3D structure of the Si/C paper electrode occur upon cycling due to the electrolyte decomposition, electrode volume expansion/contraction and electrode cracking.

2. Experimental

2.1. Materials

Ball-milled Si powder was used as active material. Si powder (99.999%, 20 mesh, Materion) was milled under argon atmosphere for 20 h using a SPEX 8000 mixer with a ball-to-powder mass ratio of 5:1. The as-milled Si powder consists of micrometric agglomerates (median size $\sim 6 \mu\text{m}$) made of sub-micrometric particles more or less welded together. More details on the characteristics of the as-milled Si powder are presented elsewhere [18]. During the slurry mixing for the electrode preparation (see below), the Si agglomerates are broken, resulting in a Si powder with a median diameter of $\sim 0.2 \mu\text{m}$ [19]. Super P carbon black (CB) (particle size $\sim 40 \text{ nm}$, Timcal) was used as the conductive additive. Carboxymethyl cellulose (CMC) (DS = 0.7, $M_w = 90\,000 \text{ g mol}^{-1}$, Sigma-Aldrich) was used as binder. Citric acid and KOH salts (Sigma-Aldrich) were used to prepare a pH3 buffer solution (0.17 M citric acid + 0.07 M KOH) as slurry medium. As previously shown, the pH3 buffering promotes covalent bonding between -OH groups present on the surface of the Si particles and -COOH groups of CMC, which improves the mechanical strength and cycling performance of the Si electrode prepared on a conventional copper foil [20,21]. AvCarb EP40 carbon paper (Fuel Cell Store) was used as 3D current collector. The EP40 carbon paper consists of non-woven carbon fibers bound by a binder filled with micrometric carbon particles (see supplementary **Fig. S1**). Its mean thickness measured with a micrometer is $163 \pm 2 \mu\text{m}$ and its areal weight is $3.37 \pm 0.05 \text{ mg cm}^{-2}$.

According to its characterization by standard laboratory XRCT, its mean porosity is ~82% with a median pore size of 36 μm and a median fiber diameter of 8 μm (see supplementary **Fig. S2**).

2.2. Electrode preparation and cell assembly

A slurry was prepared by mixing 200 mg of 80 wt.% Si, 8 wt.% CMC and 12 wt.% CB in a 0.5 ml pH3 buffer solution. Mixing was performed at 500 rpm for 1 h using a Fritsch Pulverisette 7 mixer with 3 silicon nitride balls (9.5 mm diameter). The Si composite electrode was obtained by successive soakings (typically 2-3 times) of the carbon paper (0.3 cm diam. disc) in the slurry. Slurry excess was removed from the carbon paper surface by using an absorbent paper. This was followed by a short drying period of ~2 min in air at each step of impregnation. Finally, the electrode was dried at room temperature for 12 h and then at 100°C in vacuum for 2 h. Electrodes with a Si mass loading of 1.39 mg cm⁻² were selected for the present study.

A two-electrode Swagelok[®] cell made of perfluoroalkoxy alkane (PFA) polymer was designed for *in situ* XRCT experiments. A schematic representation of the cell is shown in supplementary **Fig. S3**. The cell was assembled in an argon-filled glove box and included: (i) a Si/C paper (3 mm diameter disc) working electrode; (ii) a Whatman GF/D borosilicate glass-fiber separator soaked with 20 μl of LP30 electrolyte made of 1M LiPF₆ in 1:1 ethylene carbonate/dimethyl carbonate (battery grade from BASF); (iii) a lithium foil (3 mm diameter, 1 mm thick) as counter and reference electrode. In order to ensure a better contact between the cell components, the cell was slightly compressed with a spring installed on the counter electrode side (load estimated at 6.2 N).

2.3. SEM characterization after ion polishing

Ion beam cross sectioning of the pristine Si/C paper electrode was performed using an Ilion⁺ II Gatan apparatus and then characterized by scanning electron microscopy (SEM) using a SEM FEG ZEISS Ultra 55 microscope.

2.4. In-situ synchrotron XRCT measurements

In-situ synchrotron XRCT analyses were performed on the SLS TOMCAT beamline at the Paul Scherrer Institut facility (Villigen, Switzerland). The synchrotron beam was monochromatized to 20 keV. The Si/C paper electrode was cycled at room temperature in galvanostatic mode at full capacity between 0.005 and 1 V *vs.* Li/Li⁺ at a current density of 400 mA g⁻¹ of Si both in discharge (lithiation) and charge (delithiation) using a OrigaFlex OGF500 potentiostat/galvanostat. The electrode cycling was limited to the first discharge, first charge and second discharge. Longer cycling was not possible due to a limited amount of beam time allocated for these experiments. XRCT analyses were performed at successive intervals of 30 min. During these acquisition periods, the cell was left at the open circuit potential. A set of 1001 2D projections along a 180° cell rotation with 700 ms of exposure per projection was acquired for each XRCT scan, corresponding to a scan duration of ~12 min. 3D tomographic volumes of 417×417×170 μm³ were collected with an isotropic voxel size of 0.163 μm (meaning a resolution of 0.326 μm). They were reconstructed in 32 bit floating point representation from 2D projections using optimized software based on Fourier methods and an ImageJ plug-in user interface [22-24]. For each collected tomographic volume, a sub-volume of 293×293×137 μm³ was chosen in order to consider the exact same volume during the cycling. The look up table (LUT) is inverted on images, meaning that a voxel gets brighter when it attenuates the beam. Image processing and analysis were realized with the Fiji software [25]. The procedure is detailed in the Supporting Information (SI).

3. Results and discussion

3.1. Morphology of the pristine electrode

Fig. 1 shows cross-sectional SEM micrographs at low and high magnifications of the pristine Si/C paper electrode before cell assembly. At high magnification (**Fig. 1b**), the carbon fibers and irregular shaped Si particles are well discernable. The CMC binder and CB particles are hardly identifiable. The Si particles seem to be rather well dispersed within the C paper porous matrix and well connected to the carbon fibers. Pores of various sizes are also observed.

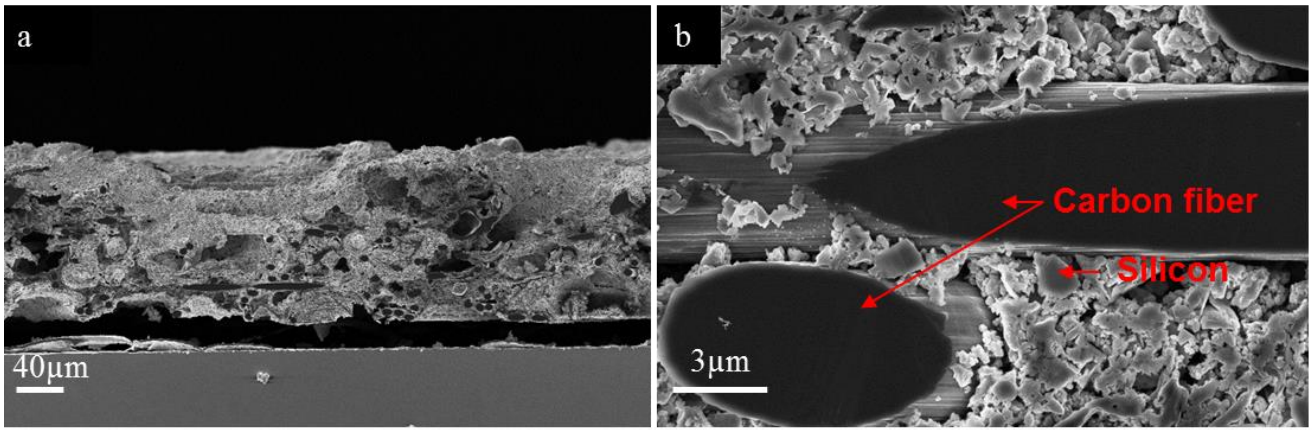


Fig. 1. Cross-sectional SEM images at (a) low and (b) high magnifications of the pristine Si/C paper electrode

In order to characterize the 3D morphology of the pristine Si/C paper electrode, synchrotron XRCT analysis has been performed after cell assembly. According to the image segmentation procedure as described in SI, three phases can be identified: (i) the solid phase (*i.e.*, C fibers + Si + CB + CMC). Note that this phase also includes some pores at the interstices between the Si and CB particles, which cannot be segmented due to their size lower than the present XRCT resolution of 0.3 μm ; (ii) the electrolyte phase (*i.e.*, the pores filled with electrolyte); and (iii) the gas phase (*i.e.*, the electrolyte-free pores). 3D views of these 3 phases for a reconstructed volume of about $300 \times 300 \times 100 \mu\text{m}^3$ are shown in **Fig. 2a, b, and c**, respectively. Their respective volume fractions in the pristine electrode are estimated to be 55, 44 and 1%. The median diameter of the electrolyte-filled pores and electrolyte-free pores is 6.1 and 4.7 μm , respectively. The very low (1%) volume fraction of electrolyte-free pores in the pristine electrode confirms its nearly total impregnation by the electrolyte. Curves showing the distribution of the total pore volume fraction along the x , y and z axes are plotted in **Fig. 2d**. One can first note that the thickness (z axis) of the pristine electrode is reduced to $\sim 90 \mu\text{m}$ after the cell assembling (as against $\sim 160 \mu\text{m}$ before assembling), indicating that the Si/C paper electrode is compressed by the cell spring. Some inhomogeneity in the pore volume distribution is also observed, especially along the electrode thickness. The increase of the porosity in the middle part of the electrode thickness may be attributed to the inhomogeneous filling of the C paper by the (Si+CB+CMC) slurry, which tends to accumulate into the outermost parts of the C paper. This

suggests that further work should be done for optimizing the filling procedure (soaking) of the hydrophobic C paper by the water-based (Si+CB+CMC) ink.

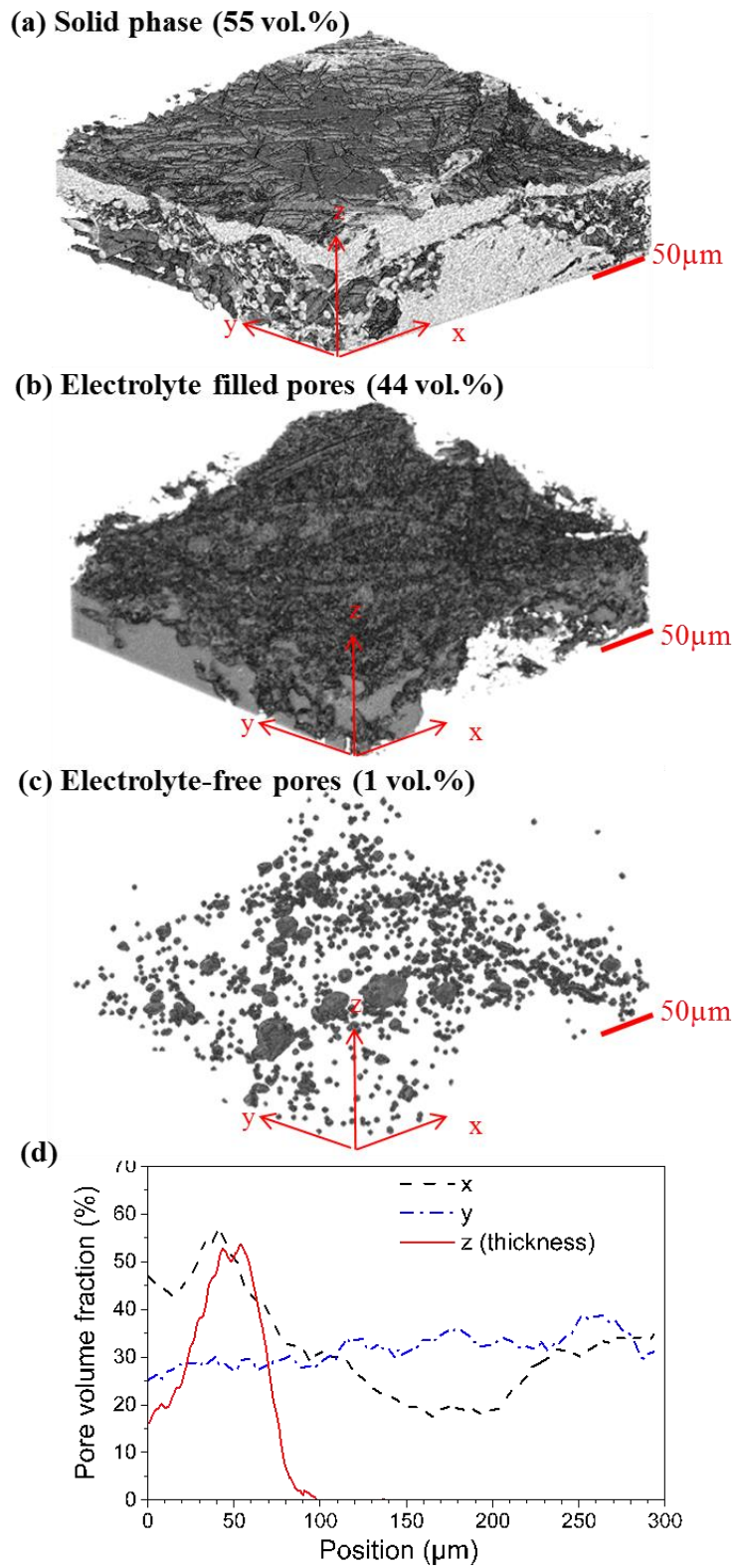


Fig. 2. 3D views of the (a) solid phase (C fibers + Si + CB + CMC), (b) electrolyte filled pores, (c) electrolyte-free pores and (d) distribution of the total pore volume fraction along the x , y , and z axes.

3.2 Qualitative analysis of the morphological evolution of the electrode upon cycling

Fig. 3a shows the evolution of the potential of the Si/C paper electrode upon cycling. During the first discharge, a potential plateau ascribed to the Si lithiation is observed at ~ 0.1 V whereas a more sloping curve centered at ~ 0.4 V corresponding to the Si delithiation is observed during the first charge, as usually observed with ball-milled Si-based electrodes [18]. During the second discharge, the decrease of the potential is more gradual than during the first discharge, indicative of a more progressive lithiation process due to the amorphization of Si during the first cycle [2]. The periodic slight increases (decreases) of the discharge (charge) potential observed in **Fig. 3a** are due to the current interruptions during the XRCT acquisition periods. From **Fig. 3a**, a capacity of 1030, 685 and 770 mAh g⁻¹ of electrode is determined for the first discharge, first charge and second discharge, respectively. The areal and volume capacities of the electrode for the first discharge are 4.9 mAh cm⁻² and 544 mAh cm⁻³, respectively. After subtraction of the capacity originating from the C paper (see the SI for more detail), the first discharge capacity is estimated to be 2884 mAh g⁻¹ of Si, corresponding to 81% of the theoretical specific capacity of Si (3579 mAh g⁻¹ for Li₁₅Si₄). This suggests that initially, a large number of the Si particles are electrochemically accessible in the 3D C paper substrate. However, it decreases to $\sim 55\%$ during the subsequent 1st charge and 2nd discharge because of the electronic or ionic isolation of some Si particles associated with the morphological change of the electrode upon cycling as described below.

Fig. 3b shows XRCT slice images acquired at different cycling times identified by the numbers 1 to 8 in **Fig. 3a**. For each of these different lithiation or delithiation states, images in the transversal (x,z) plane (*i.e.* through the electrode thickness) and in the lateral (x,y) plane are shown in **Fig. 3b**. At the bottom of the electrode, *i.e.* at $z = 0$, the stainless steel connector is recognizable as the bright spot. The interface between the top of the electrode and the bottom of the separator is represented by the red dashed line on the transversal images. The green dashed line corresponds to the z position of the lateral images presented below. The corresponding XRCT video in the through-

thickness plane is available in the SI (see **movie 1**). On the basis on the XRCT analysis, the following phenomena can be highlighted.

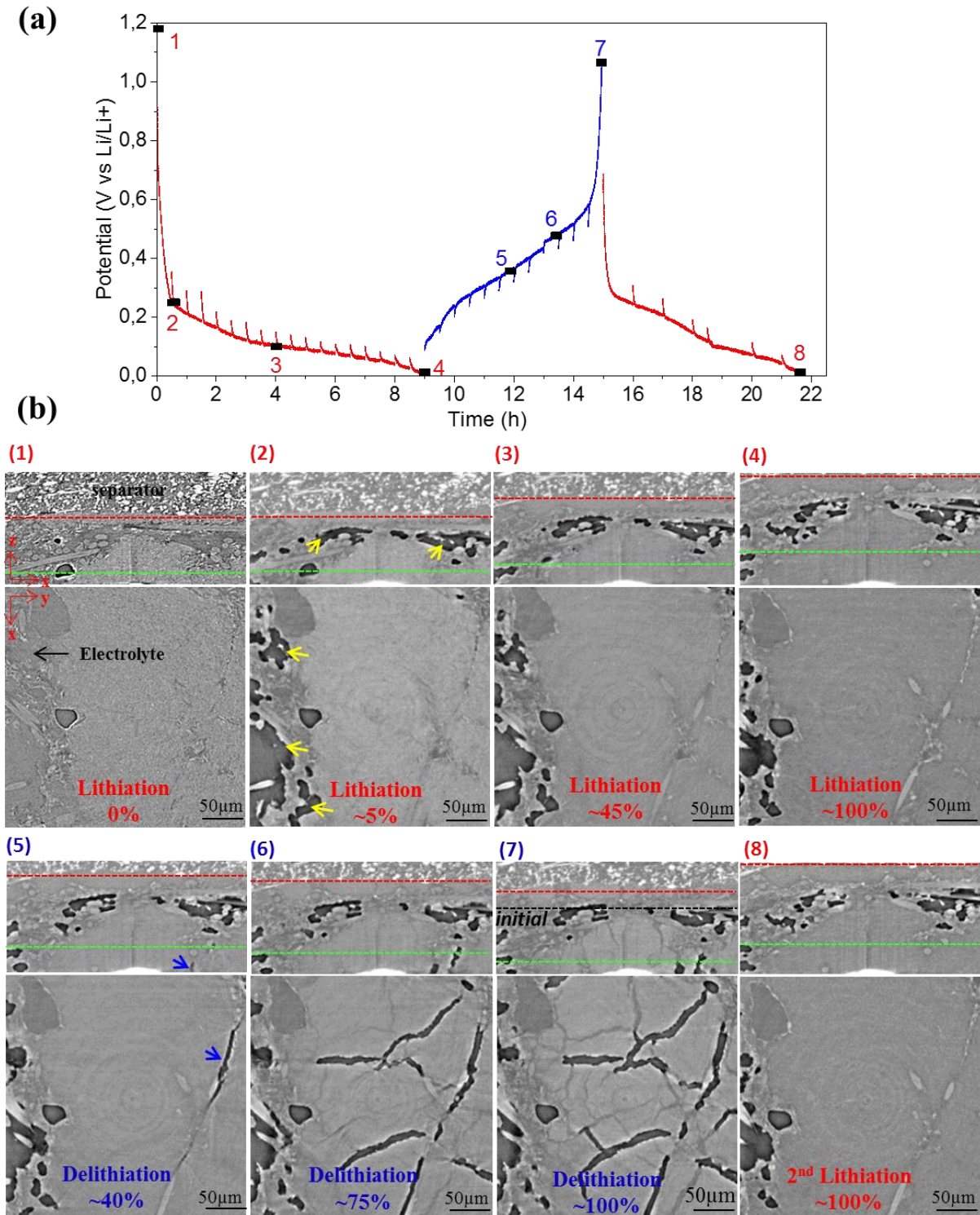


Fig. 3. (a) Evolution of the potential of the Si/C paper electrode during the 1st discharge, 1st charge and 2nd discharge; (b) XRCT slice images in the transversal (x,z) and lateral (x,y) planes of the Si/C paper electrode for different cycling stages corresponding to the numbers 1-8 indicated on the potential curve. The red dashed line on the transversal (x,z) images sets the interface between the top of the electrode and the bottom of the separator. The green dashed line corresponds to the z position of the lateral (x,y) images shown below. The images are in Paganin phase contrast mode, except for step (1) images which are in attenuation contrast mode.

Electrode expansion/contraction. – As seen in **Fig. 3b**, the displacement of the red dash line, indicating the top of the electrode, allows us to visualize the electrode thickness expansion/contraction resulting from its lithiation/delithiation (this is also clearly observable in **movie 1**). One can note that at the end of the first cycle (step 7), the red dash line does not come back to its initial (step 1) position indicated by the black dash line. This means that an irreversible expansion of the electrode occurs. A precise quantification of the electrode expansion/contraction is presented later. The darkening of the solid phase upon discharging (steps 1-4) is also visible on the images, indicating a decrease of the X-ray absorption of the solid phase which becomes less dense as the electrode is lithiated. As expected, the reverse is observed during the charge (steps 5-7).

Gas evolution. – At the beginning of the discharge, darker zones (see yellow arrows on step 2 images in **Fig. 3b**) appear in some porous regions initially filled with the electrolyte. These low X-ray absorbing zones may be attributed to the formation of gas bubbles (*e.g.*, H₂, C₂H₄, CO₂) related to the electrolyte decomposition [26,27]. The formation of gas bubbles and channels was also recently observed by Sun et al. from *in-situ* synchrotron XRCT with a conventional Si/Cu foil electrode [13]. As seen on the transversal images in **Fig. 3b**, the gas channels seem to be essentially formed during the first stage of the discharge, which is consistent with the fact that the reductive electrolyte decomposition is well known to occur in this potential range. They tend to accumulate in the middle part of the electrode thickness, *i.e.* where the electrode is initially more porous (see **Fig. 2d**). **These gas channels can be observed during all the electrode cycling in Fig. 3b, which suggests that the produced gas bubbles do not escape from the electrode and thus are not replaced with electrolyte.** However, this may not occur at the edges of the electrode (zones not imaged here), where the generated gas would more easily migrate out of the electrode.

SEI formation. – The electrolyte decomposition also results in the formation of solid compounds, such as (CH₂OCO₂Li)₂ and Li₂CO₃ [28]. These products accumulate in the electrode pores at each cycle since the SEI layer is mechanically unstable due to the Si volume change [29]. In order to visualize this process, XRCT images have been focused in an electrode zone displaying large

electrolyte-filled pores and for different cycling stages as shown in **Fig. 4a-d**. At 5% of lithiation (**Fig. 4b**), the formation of a large gas pore is noticeable as reported before. We can also observe the formation of a thin brighter (denser) layer at the interface between the electrolyte and the Si-based composite at the end of the 1st lithiation, indicated by the green arrow on **Fig. 4c**. It is hazardous to give a precise value of its thickness due to edge effects. However, it is possible to observe qualitatively the growth of this SEI layer between the 1st lithiation (**Fig. 4c**) and the 2nd lithiation (**Fig. 4d**). A thin SEI layer must also be formed around the Si particles dispersed in the solid phase of the electrode but it is not visible here due to the insufficient resolution of the present XRCT analysis.

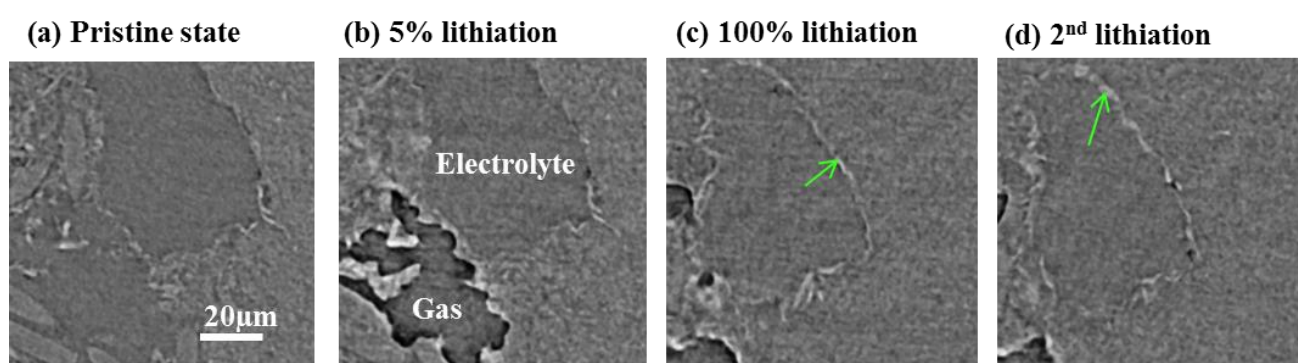


Fig. 4. XRCT slice images in the (x, y) plane of the Si/C paper electrode at different cycling stages: (a) pristine state; (b) after 5% lithiation; (c) at the end of the 1st lithiation; (d) at the end of the 2nd lithiation. The images are in X-ray attenuation contrast mode.

Electrode cracking. – As seen in **Fig. 3b**, cracks first appear in the bottom part of the electrode after 40% of delithiation (see blue arrows on step 5 images). Additional XRCT images acquired for different delithiation states at the top, middle and bottom parts of the electrode (**Fig. 5**) confirm that the cracks are initially formed in the bottom part of the electrode. This may be due to the nearby presence of the rigid stainless steel connector and to the larger volume change in the bottom part of the electrode (see **Fig. 6b**), accentuating the mechanical constraints on this part of the electrode. After 75% of delithiation, the cracks spread across the entire volume of the electrode and their density increases drastically until reaching a significant part of the total electrode volume at the end of the charge. Noticeably, cracks are either filled with electrolyte (in dark gray) or with gas (in black). However, in the top area of the electrode, all the cracks are filled with electrolyte (**Fig. 5**) as the latter

can easier percolate from the separator. After the second discharge (see step 8 images in **Fig. 3b**), the electrode has expanded again and the cracks formed during the previous charge are reclosed by the Si volume expansion. Such a behavior has also been observed from *post-mortem* SEM observations on some conventional Si/Cu foil electrodes [30]. Actually, the electrode cracking observed during its delithiation (volume contraction) can be interpreted as the consequence of the rupture of Si-CMC bonds upon its lithiation (volume expansion). The resulting less cohesive electrode then becomes unable to mechanically resist the Si volume contraction and its cracking occurs upon charging. Nonetheless, it is important to stress that this cracking process is reversible since the electrode recovers the same morphology after the 1st and 2nd lithiation (see step 8 images *versus* step 4 images in **Fig. 3b**). However, it must be noted that the irreversible cracking of the Si particles (assumed to mainly occur during the first discharge from acoustic emission measurements [31]) as well as their irreversible disconnection from the C fibers and CB particles (electrical network rupture) are not discernable here due to the insufficient resolution of the present XRCT analyses

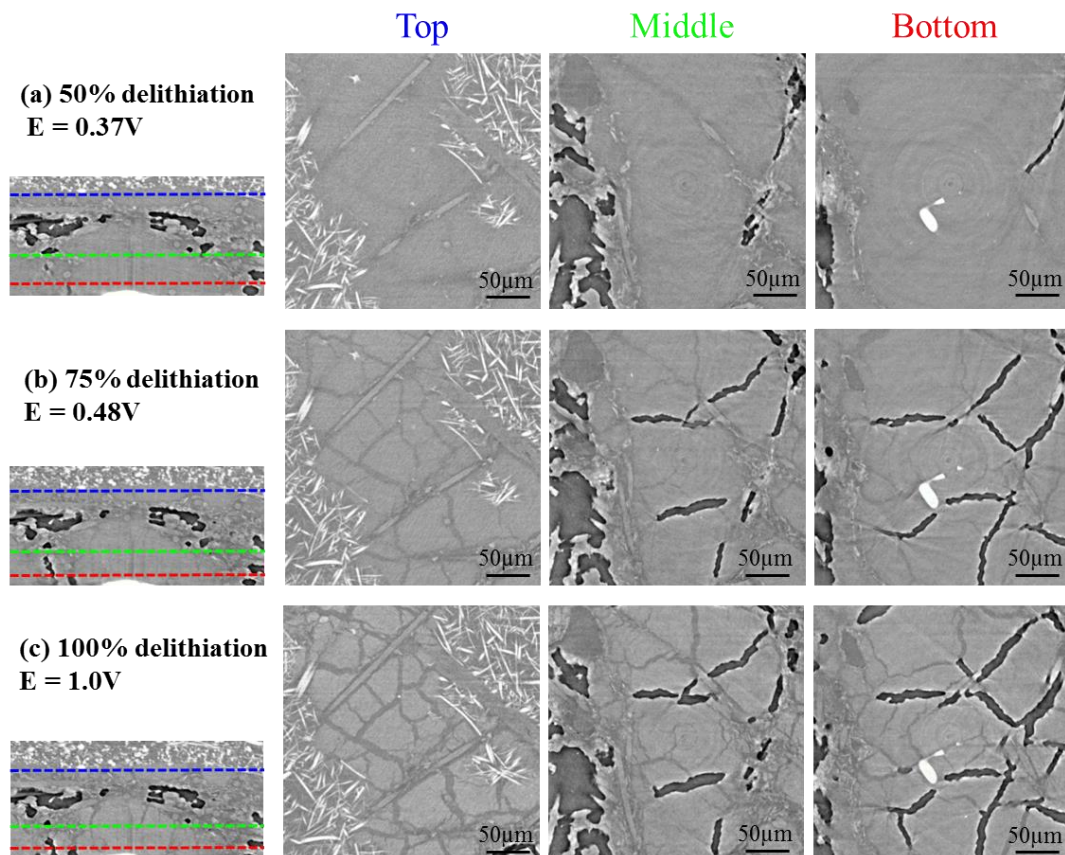


Fig. 5. XRCT images acquired for different delithiation states at the top, middle and bottom parts of the Si/C paper electrode. The dash lines on the transversal (x,z) images (at left) set the different z positions of the lateral (x,y) images (at right). The images are in Paganin phase contrast mode.

3.3 Quantitative analyses of the morphological evolution of the electrode upon cycling

3.3.1 Electrode dimensional changes

As reported before, the Si/C paper electrode undergoes important thickness variation during cycling. **Fig. 6a** describes the dimensional change of the Si/C composite electrode along the three Cartesian axes. The relative changes in lateral (x , y) directions are calculated from the displacement of reference points taken inside the electrode volume at different z values. The relative change in the transversal (z) direction is calculated from the displacement of the separator / electrode interface. First, it appears that the dimensional change of the electrode is anisotropic. At the end of the 1st lithiation a relative expansion $\frac{dz}{z_0} = 64\%$ in the transversal direction, compared to $\frac{dx}{x_0} = 21\%$ and $\frac{dy}{y_0} = 11\%$ in the lateral directions. The lower lateral expansion of the electrode can be explained by the fixed lateral dimensions of the electrochemical cell restricting the electrode in-plane displacement. By contrast, the out-of-plane expansion of the electrode is easier due to the flexibility of the separator. This can also be partially explained by an anisotropic structuring effect of the carbon paper fibers as they are primarily parallel to the plane of the carbon paper (see **Fig. S2**). This can strengthen the electrode in the (x , y) plane and thus lower the dilatation in these directions. At the end of the 1st delithiation, a residual expansion of $\frac{dz}{z_0} = 24\%$, $\frac{dx}{x_0} = 11\%$ and $\frac{dy}{y_0} = 6\%$ is observed, confirming that the electrode expansion is partially irreversible. However, it must be noted that the expansion/contraction of the presence 3D Si/C paper electrode is lower and more reversible than with a conventional 2D Si/Cu foil electrode configuration. Indeed, from electrochemical dilatometry measurements, the latter displayed a maximal thickness expansion of $\sim 170\%$ and an irreversible thickness expansion of $\sim 50\%$ for the first cycle, despite its $\sim 40\%$ lower Si areal mass loading (0.9 mg cm^{-2}) [21].

Fig. 6b shows the relative change with cycling of the electrode volume for different zones along its thickness as shown in the transversal (x , z) image of the electrode at the initial state in **Fig.**

6c, namely (i) a bottom zone (*i.e.* between $z_0 = 0$ and $\sim 25 \mu\text{m}$), (ii) a middle zone (*i.e.* between $z_0 = \sim 25$ and $\sim 65 \mu\text{m}$), and (iii) a top zone (*i.e.* between $z_0 = \sim 65$ and $\sim 90 \mu\text{m}$). Their pore volume fractions in the initial state are *ca.* 20, 50 and 20%, respectively. The volume change with cycling of these different parts of the electrode is determined from the displacement of the reference planes $z_0 = 25$, 65 and 90 μm identified from the characteristic shape of some objects (*e.g.* C fibers) present in these reference planes. Displacements in the x and y directions are also considered for calculation of the volume changes in these three zones. The total volume change of the electrode is also presented in **Fig. 6b**. It appears that the relative volume expansion of the bottom part of the electrode during the 1st discharge is much larger than for the middle and top parts, with maximum volume expansions of 151, 73 and 73%, respectively. The higher volume expansion of the bottom zone may be due its low initial porosity of 20% (meaning a higher volume fraction of Si active material) but also because of the nearby presence of the rigid stainless steel connector, which constrains its transversal expansion only towards the top of the electrode. In contrast, the volume expansion of the initially more porous (50%) middle part of the electrode can be significantly buffered by the surrounding large pores. Regarding the top part of the electrode, its transversal expansion is probably limited by the compressive strain exerted from below by the electrode expansion and from above by the presence of the separator. This limitation is highlighted by the presence of a plateau in the volume expansion of the top zone from ~ 8 h of discharge. At the end of the 1st charge, an irreversible expansion is observed for the three zones but it is larger for the bottom zone (71%) than for the middle and top zones ($\sim 33\%$). This suggests that irreversible change in the electrode structure and the related disconnections of the Si particles (preventing their delithiation) are more intense in the bottom part of the electrode.

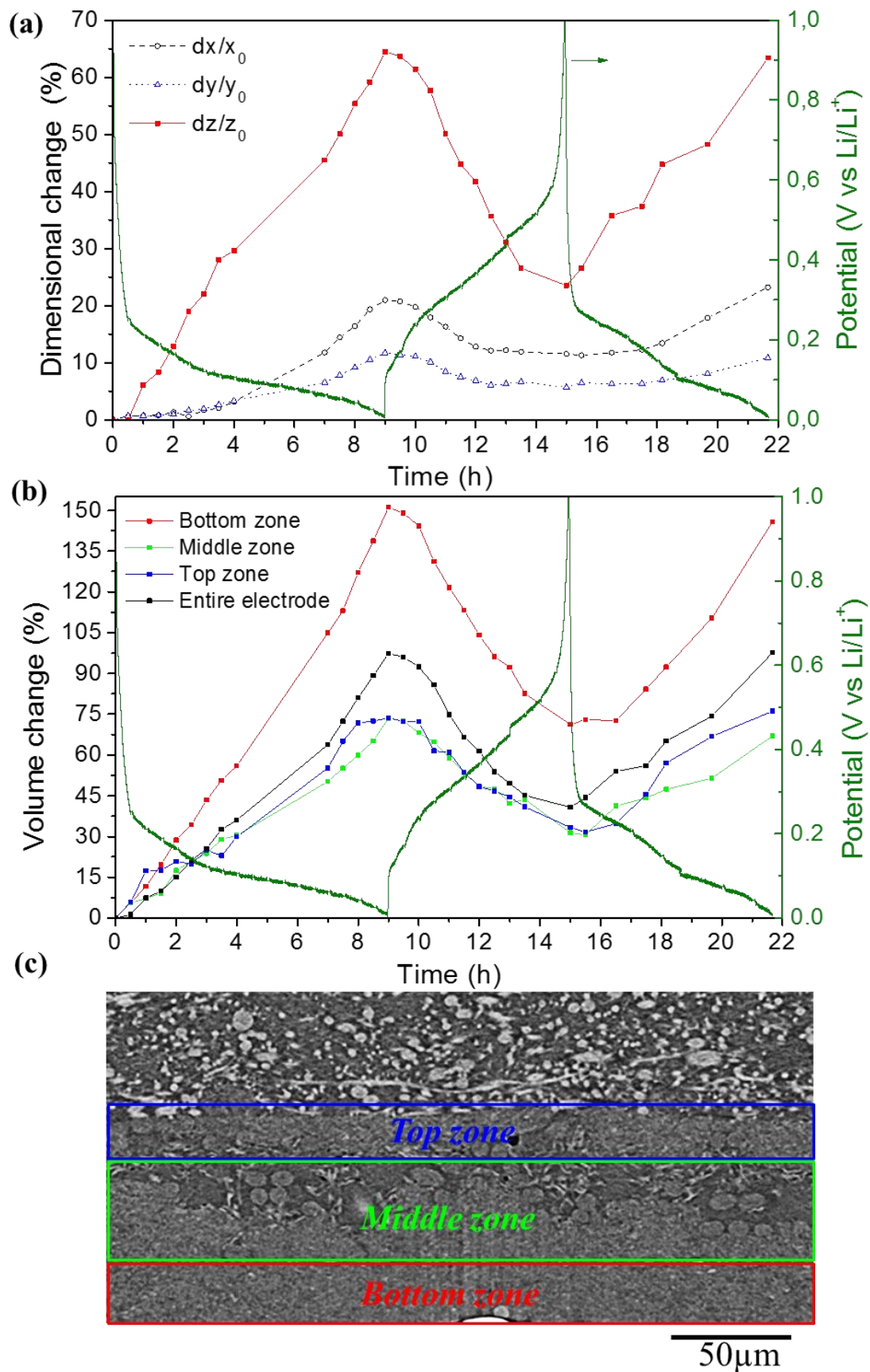


Fig. 6. Relative change with cycling of (a) the lateral and transversal dimensions of the electrode, and (b) the electrode volume for different zones along its thickness represented in (c) from a transversal (x,z) image of the electrode in its initial state.

3.3.2 Phase volume fraction changes

Fig. 7 shows the evolution upon cycling of the volume fractions of the solid, electrolyte (electrolyte-filled pores) and gas (electrolyte-free pores) phases in the Si/C electrode. During the first 30 min of discharge, one can observe an abrupt decrease of the electrolyte volume fraction from 44 to 23%, while the volume fractions of the gas phase and solid phase increase from 1 to 11% and from 55 to 66%, respectively. As previously discussed, this can be attributed to the reductive electrolyte decomposition occurring in this potential range (*i.e.* between 1 and 0.25 V) that induces the formation of gaseous and insoluble products. Nearly no change in the volume fraction of the gas phase is observed during the rest of the 1st discharge, confirming that the electrolyte decomposition mainly occurs during the initial stage of the discharge. On the other hand, the volume fraction of the solid phase progressively increases during the discharge due to the Si volume expansion induced by its lithiation. The reverse is observed for the electrolyte phase, reflecting the decrease of the electrode porosity by the swelling of the Si particles. Note that an abrupt increase (decrease) of the solid (electrolyte) volume fraction is observed at $t \sim 7.5$ h ($E \sim 50$ mV). However, the reproducibility of this event needs to be confirmed. If significant, it may originate from an intensification of the Si particle cracking due to the formation of the well-known crystalline $\text{Li}_{15}\text{Si}_4$ phase at 50 mV [2]. However, it should also result in a sudden increase of the gas volume fraction due to the formation of fresh reactive Si surface, which is not observed here.

During the charge, one can observe as expected an overall decrease of the volume fraction of the solid phase (from 72 to 57%) as the Si particles deflate with their delithiation while the opposite is observed for the electrolyte phase (increase from 19 to 29%). However, sudden variations in the volume fractions of the electrolyte and solid phases can be detected, especially around half of the charge. An increase of the gas volume fraction is also observed from half of the charge. These variations may be related to the electrode cracking inducing major changes in the electrode morphology as previously discussed. At the second discharge, the solid volume fraction increases

again (from 57 to 82%) concomitantly to the decrease of the electrolyte volume fraction (from 29 to 11%).

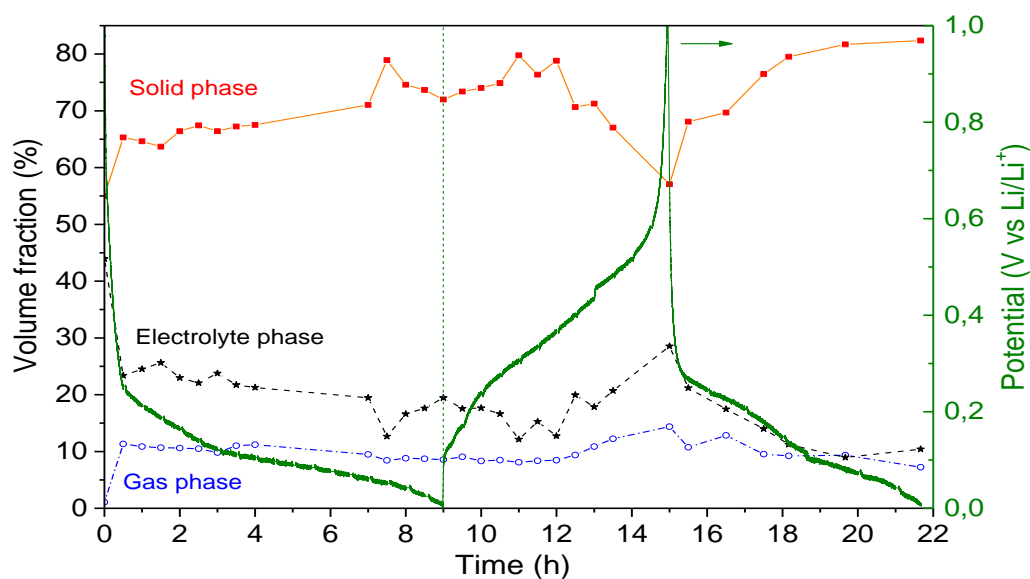


Fig. 7. Evolution with cycling of the volume fractions of the solid, electrolyte and gas phases in the Si/C paper electrode.

3.3.3. Evolution of the pore size and connectivity

As previously shown, major changes in the porous structure of the Si/C paper electrode occur upon cycling due to the electrolyte decomposition (gas evolution), electrode volume change and electrode cracking. In order to characterize the morphological evolution of the electrode porous network, the size (diameter) and connectivity of the electrolyte-filled and gas-filled pores have been evaluated at different cycling stages as summarized in **Table 1**. Pore size and connectivity were calculated according to the procedure detailed in SI. Remember that this characterization is limited to the pores having a diameter $\geq \sim 0.3 \mu\text{m}$. **Fig. 8** presents the size distribution curves and corresponding 3D views of the electrolyte-filled pores (**Fig. 8a-b**) and electrolyte-free pores (**Fig. 8c-d**) of the Si/C paper electrode before cycling and after the 1st discharge, 1st charge and 2nd discharge. Regarding the electrolyte-filled pores, they maintain a high connectivity ($\geq 80\%$) upon cycling despite major changes in the electrode morphology. However, a significant decrease of their size and volume fraction can be observed with cycling. For the electrolyte-free pores, their connectivity is lower ($\leq 61\%$) and thus a significant part of these pores are closed in contrast to the electrolyte-filled pores.

Their size stabilizes at $\sim 9 \mu\text{m}$ from the 1st discharge whereas the size of the electrolyte-filled pores fluctuates with cycling.

	Electrolyte-filled pores			Electrolyte-free pores		
	Median size (μm)	Connectivity (%)	Vol. fraction (%)	Median size (μm)	Connectivity (%)	Vol. fraction (%)
Pristine	6.1	93	44	4.7	14	1
1st discharge	2.7	80	20	8.9	61	9
1st charge	3.4	98	29	8.9	45	14
2nd discharge	2.4	83	10	8.9	53	8

Table 1. Median size, connectivity and volume fraction of the electrolyte-filled and electrolyte-free pores in the Si/C paper electrode before cycling and after the 1st discharge, 1st charge and 2nd discharge.

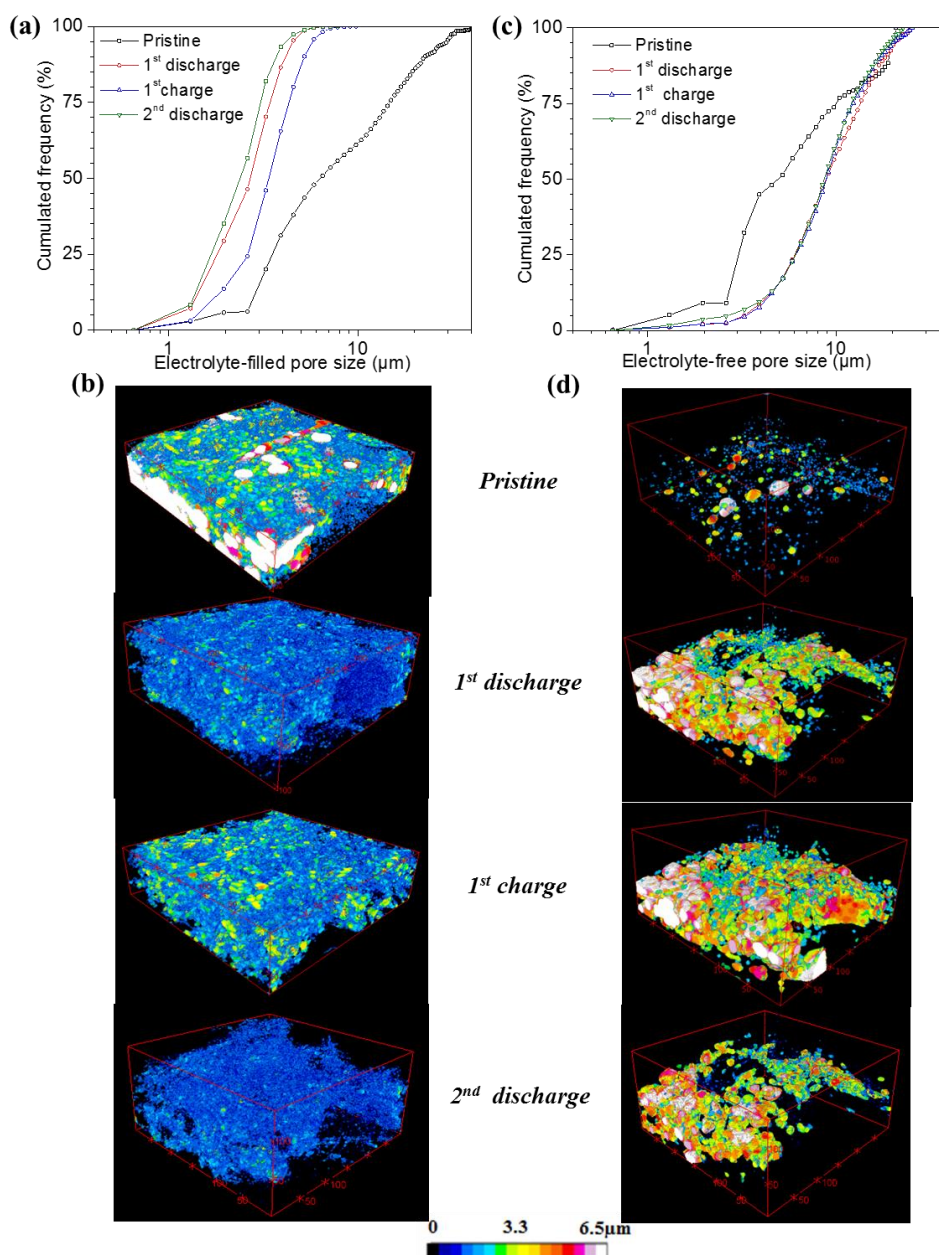


Fig. 8. (a, c) Size distribution curves and (b, d) corresponding color-scale 3D views of the electrolyte-filled pores (a, b) and electrolyte-free pores (c, d) of the Si/C paper electrode before cycling and after the 1st discharge, 1st charge and 2nd discharge.

4. Conclusion

This study has shown that valuable information on the morphological changes upon cycling of a flexible 3D Si/C paper electrode can be obtained by *in-situ* XRCT. For the pristine electrode, it appears that the (Si+CB+CMC) loading is lower in the center part of the electrode thickness, the electrode is compressed in thickness during the cell assembling, and the filling of its porous network by the electrolyte is nearly complete. The formation of gas channels attributed to the reductive electrolyte decomposition is observed at the beginning of the 1st discharge. The growth of an SEI layer is also discernable. The electrode cracking initiates during the 1st charge from the bottom of the electrode. These large cracks, filled with electrolyte or gas, close during the subsequent discharge. The dimensional expansion/contraction of the electrode is anisotropic with a much larger variation in the transverse direction. Moreover, it is larger and less reversible in the bottom part of the electrode, suggesting that irreversible change in the electrode structure and the related disconnections of the Si particles are more intense in this part of the electrode.

The cracking of the Si particles and their disconnection from the electronic or ionic network could not be characterized here due to the insufficient spatial and phase-contrast resolutions of the present XRCT experiments. Further work at higher XRCT resolution is planned in the near future for this purpose. Multiscale XRCT data will be highly useful for optimizing the Si electrode formulation and processing as well as the electrolyte composition.

Acknowledgments

The authors thank the Natural Sciences and Engineering Research Council (NSERC) of Canada for supporting this work. The authors also thank J. Adrien and M. Mokhtari for their precious help during the *in-situ* XRCT measurements at the Tomcat beamline (SLS facility, Villigen Switzerland) and N. Vaché for the electrode ionic polishing.

References

- [1] M.N. Obrovac, L. Christensen, Structural changes in silicon anodes during lithium insertion-extraction, *J. Electrochem. Soc.* 7 (2004) A93-A96.
- [2] J. Li, J.R. Dahn, An in situ x-ray diffraction study of the reaction of Li with crystalline Si, *J. Electrochem. Soc.* 154 (2007) A156-A161.
- [3] M.N. Obrovac, L.J. Krause, Reversible cycling of crystalline silicon powder, *J. Electrochemical Soc.* 154 (2007) A103-A108.
- [4] J.R. Szczech, S. Jin, Nanostructured silicon for high capacity lithium battery anodes, *Energy Environ. Sci.* 4 (2011) 56-72.
- [5] X. Su, Q. Wu, J. Li, X. Xiao, A. Lott, W. Lu, B.W. Sheldon, J. Wu, Silicon-based nanomaterials for lithium-ion batteries: A Review, *Adv. Energy Mater.* 4 (2014) 1300882.
- [6] T. Wada, T. Ichitsubo, K. Yubuta, H. Segawa, H. Yoshida, H. Kato, Bulk-nanoporous-silicon negative electrode with extremely high cyclability for lithium-ion batteries prepared using a top-down process, *Nano Lett.* 14 (2014) 4505–4510.
- [7] D. Mazouzi, D. Reyter, M. Gauthier, P. Moreau, D. Guyomard, L. Roué, B. Lestriez, Very high surface capacity observed with Si negative electrodes embedded in copper foam as 3D current collector, *Adv. Energy Mater.* 4 (2014) 1301718.
- [8] H. Wolf, Z. Pajkic, T. Gerdes, M. Willert-Porada, *J. Power Sources* 190 (2009) 157-161.
- [9] Y. Fu, A. Manthiram, Silicon nanoparticles supported on graphitic carbon paper as a hybrid anode for Li-ion batteries, *Nano Energy* 2 (2013) 1107-1112.
- [10] J. K. Lee, K. B. Smith, C. M. Haynerb, H. H. Kung, Silicon nanoparticles–graphene paper composites for Li ion battery anodes, *Chem. Commun.* 46 (2010) 2025–2027.
- [11] F. Tariq, V. Yufit, D. S. Eastwood, Y. Merla, M. Biton, B. Wu, Z. Chen, K. Freedman, G. Ofeer, E. Peled, P. D. Lee, D. Golodnitsky, and N. Brandon, In-Operando X-ray Tomography Study of Lithiation Induced Delamination of Si Based Anodes for Lithium-Ion Batteries, *ECS Electrochem. Lett.* 3 (2014) A76-A78.

- [12] J. Gonzalez, K. Sun, M. Huang, J. Lambros, S. Dillon, I. Chasiotis, Three dimensional studies of particle failure in silicon based composite electrodes for lithium ion batteries, *J. Power Sources* 269 (2014) 334-343.
- [13] F. Sun, H. Markötter, I. Manke, A. Hilger, N. Karddjilov, J. Banhart, Three-Dimensional Visualization of Gas Evolution and Channel Formation inside a Lithium-Ion Battery, *ACS Appl. Mater. Interfaces* 8 (2016) 7156–7164.
- [14] F. Sun, H. Markötter, K. Dong, I. Manke, A. Hilger, N. Karddjilov, J. Banhart, Investigation of failure mechanisms in silicon based half cells during the first cycle by micro X-ray tomography and radiography, *J. Power Sources* 321 (2016) 174-184.
- [15] J.M. Paz-Garcia, O.O. Taiwo, E. Tudisco, D.P. Finegan, P.R. Shearing, D.J.L Brett, S.A. Hall, 4D analysis of the microstructural evolution of Si-based electrodes during lithiation: Time-lapse X-ray imaging and digital volume correlation, *J. Power Sources* 320 (2016) 196-203.
- [16] P. Pietsch, M. Hess, W. Ludwig, J. Eller, V. Wood, Combining operando synchrotron X-ray tomographic microscopy and scanning X-ray diffraction to study lithium ion batteries, *Sci. Rep.* 6 (2016) 27994.
- [17] D.S Eastwood, R.S. Bradley, F. Tariq, S.J. Cooper, O.O. Taiwo, J. Gelb, A. Merkle, D.J.L. Brett, N.P. Brandon, P.J. Withers, P.D. Lee, P.R. Shearing, The application of phase contrast X-ray techniques for imaging Li-ion battery electrodes, *Nucl. Instrum. Methods Phys. Res. B* 324 (2014) 118-123.
- [18] M. Gauthier, D. Mazouzi, D. Reyter, B. Lestriez, P. Moreau, D. Guyomard, L. Roué, A low-cost and high performance ball-milled Si-based negative electrode for high-energy Li-ion batteries, *Energy Environ. Sci.* 6 (2013) 2145-2155.
- [19] Z. Karkar, D. Mazouzi, C. Reale Hernandez, D. Guyomard, L. Roué, B. Lestriez, Threshold-like dependence of silicon-based electrode performance on active mass loading and nature of carbon conductive additive, *Electrochim. Acta* 215 (2016) 276-288.

- [20] D. Mazouzi, B. Lestriez, L. Roué, D. Guyomard, Silicon composite electrode with high capacity and long cycle life, *Electrochem. Solid-State Lett.* 12 (2009) A215-A218.
- [21] A. Tranchot, H. Idrissi, P. X. Thivel, L. Roué, Impact of the slurry pH on the expansion/contraction behavior of silicon/carbon/carboxymethylcellulose electrodes for Li-ion batteries, *J. Electrochem. Soc.* 163 (2016) A1020-A1026.
- [22] C. Hintermüller, F. Marone, A. Isenegger, M. Stampanoni, Image processing pipeline for synchrotron-radiation-based tomographic microscopy, *J. Synchrotron Rad.* 17 (2010) 550-559.
- [23] F. Marone, B. Münch, M. Stampanoni, Fast reconstruction algorithm dealing with tomography artifacts, *Proc. SPIE 7804, Developments in X-Ray Tomography VII*, 780410 (2010).
- [24] F. Marone, M. Stampanoni, Regridding reconstruction algorithm for real time tomographic imaging, *J. Synchrotron Rad.* 19 (2012) 1029-1037.
- [25] J. Schindelin, I. Arganda-Carreras, E. Frise, V. Kaynig, M. Longair, T. Pietzsch, S. Preibisch, C. Rueden, S. Saalfeld, B. Schmid, J.Y. Tinevez, D. J. White, V. Hartenstein, K. Eliceiri, P. Tomancak, A. Cardona, Fiji: an open-source platform for biological-image analysis, *Nat Methods* 9 (2012) 676-682.
- [26] J. Yang, N. Solomatin, A. Kraytsberg, Y. Ein-Eli, In Situ spectro-electrochemical insight revealing distinctive silicon anode solid electrolyte interphase formation in a lithium-ion battery, *ChemistrySelect* 3 (2016) 572-576.
- [27] M. Holzapfel, H. Buqa, L.J. Hardwick, M Hahn, A. Würsig, W. Scheifele, P. Novák, R. Kötz, C. Veit, F.M. Petrat, Nano silicon for lithium-ion batteries, *Electrochim. Acta* 52 (2006) 973-978.
- [28] V. Etacheri, O. Haik, Y. Goffer, G.A. Roberts, I.C. Stefan, R. Fasching, D. Aurbach, Exceptional electrochemical performance of Si-nanowires in 1,3-dioxolane solutions: a surface chemical investigation, *Langmuir* 28 (2012) 6175-6184.
- [29] D. Mazouzi, N. Delpuech, Y. Oumellal, M. Gauthier, M. Cerbelaud, J. Gaubicher, N. Dupré, P. Moreau, D. Guyomard, L. Roué, B. Lestriez, New insights into the silicon-based electrode's

irreversibility along cycle life through simple gravimetric method, *J. Power Sources* 220 (2012) 180-184.

[30] A. Tranchot, H. Idrissi, P.-X. Thivel, L. Roué, Influence of the Si particle size on the mechanical stability of Si-based electrodes evaluated by in-operando dilatometry and acoustic emission, *J. Power Sources* 330 (2016) 253-260.

[31] A. Tranchot, A. Etienne, P.X. Thivel, H. Idrissi, L. Roué, In-situ acoustic emission study of Si-based electrodes for Li-ion batteries, *J. Power Sources* 279 (2015) 259-266.